Molecular Therapy
Methods & Clinical Development
Original Article

Characterization of VSV-GP morphology by cryo-EM imaging and SEC-MALS

Dongyue Xin,[1,7] Leela Kurien,[1] Katherine Briggs,[1] Adrian Schimek,[2] Richard Dambra,[3] Daniel Hochdorfer,[4] Tanja A. Arnouk,[4,8] Marija Brgles,[4] Saurabh Gautam,[2,5,9] Dominik Hotter,[4] Johannes Solzin,[4] Thomas Kriehuber,[4] Joseph Ashour,[3] Adam Vigil,[3,10] Michael Hawley,[1,11] and Xiaorong He[6]

[1]Material and Analytical Sciences, Boehringer Ingelheim Pharmaceuticals Inc., Ridgefield, CT, USA; [2]ViraTherapeutics GmbH, Innsbruck, Austria; [3]Drug Metabolism and Pharmacokinetics, Boehringer Ingelheim Pharmaceuticals Inc., Ridgefield, CT, USA; [4]Viral Therapeutics Center, Boehringer Ingelheim Pharma GmbH & Co. KG, Biberach, Germany; [5]Boehringer Ingelheim International GmbH, Ingelheim, Germany; [6]Boehringer Ingelheim Pharmaceuticals Inc., Ridgefield, CT, USA

Vesicular stomatitis virus expressing the glycoprotein of the lymphocytic choriomeningitis virus (VSV-GP) is a promising platform for oncolytic viruses and cancer vaccines. In this work, cryoelectron microscopy (cryo-EM) imaging was employed to directly visualize VSV-GP particles. Several different subpopulations of virus particle morphology were observed. Definition and fraction counting of subpopulations enabled quantitative comparison of subpopulation profiles between several VSV-GP samples. In developing an orthogonal method with higher throughput, we showed that the morphological profile of the VSV-GP particles can be characterized by size exclusion chromatography coupled with a multi-angle light scattering detector (SEC-MALS) based on a novel shape-based separation mechanism. Together, the two complementary techniques enable the analysis of morphological profile for VSV-GP and potentially other non-spherical viruses or nanoparticles.

INTRODUCTION

Viruses with oncolytic properties have become an attractive new modality in anti-cancer drug development.[1,2] These viruses can selectively lyse cancer cells, change the tumor microenvironment, and induce additional immune response against tumors antigens.[1] Vesicular stomatitis virus expressing the glycoprotein of the lymphocytic choriomeningitis virus (VSV-GP) is one oncolytic virus platform and cancer vaccine that has demonstrated excellent anti-tumor activities.[3–11] New analytical techniques for better characterization of VSV-GP can enhance the understanding of the structure-function relationship and serve as additional tools in process development.

The structure of VSV components, the VSV capsid, and whole virions have been investigated by X-ray crystallography,[12–19] negative staining transmission electron microscopy (TEM)[20–22] and cryoelectron microscopy (cryo-EM).[23–25] X-ray crystallography solved the fine structure of individual viral proteins and RNA-protein complexes. Previous attempts of negative staining TEM on VSV only provided limited two-dimensional structural details on intact virions.[21] Cryo-EM studies revealed how individual viral proteins assemble into the whole virion and enable the development of a structural model for VSV capsid packing.[23,26–28] Each virion capsid involves three helical layers: an inner helix formed by packing of RNA and the nucleoprotein N complex and two outer helical layers of matrix protein M, which are associated with both the inner helix and the cytoplasmic tail of envelope G proteins. Intact VSV adopts a rigid bullet-shaped morphology due to the interactions between neighboring viral proteins.[23,24]

Morphology changes and the presence of VSV subpopulations have been described previously. Besides the bullet-shaped particles (B particles), distorted or damaged B particles have been observed by negative staining TEM in VSV samples after long-term storage.[20] In addition, defective interfering particles with a truncated genome and a shorter length have been isolated and investigated for their biological function.[22,29–32] Despite these observations, there is only limited structural understanding of these particle subpopulations.[20] In this study, structural details of the subpopulations present in VSV-GP preparations were systematically investigated with cryo-EM.

Cryo-EM can clearly reveal the morphology profile of VSV-GP samples, but the technology is not readily accessible to all manufacturing facilities and organizations. In developing an orthogonal, high-throughput screening method, we employed size exclusion chromatography coupled with a multi-angle light scattering detector (SEC-MALS) for the characterization of VSV-GP particle morphology. SEC is a liquid chromatography method that separates macromolecules based

Received 11 October 2024; accepted 3 February 2025;
https://doi.org/10.1016/j.omtm.2025.101429.

[7]Present address: R&D Project Management, Boehringer Ingelheim Pharmaceuticals Inc., Ridgefield, CT, USA

[8]Present address: Probiogen AG, Herbert Bayer Strasse 8, Berlin, Germany

[9]Present address: Novartis Pharmaceutical Manufacturing GmbH, Biochemiestrasse 10, 6336 Langkamfen, Austria

[10]Present address: Regeneron Pharmaceuticals, 777 Old Saw Mill River Rd., Tarrytown, NY, USA

[11]Present address: PharmSci Links

Correspondence: Dongyue Xin, Material and Analytical Sciences, Boehringer Ingelheim Pharmaceuticals Inc., Ridgefield, CT, USA.
E-mail: dongyue.xin@boehringer-ingelheim.com

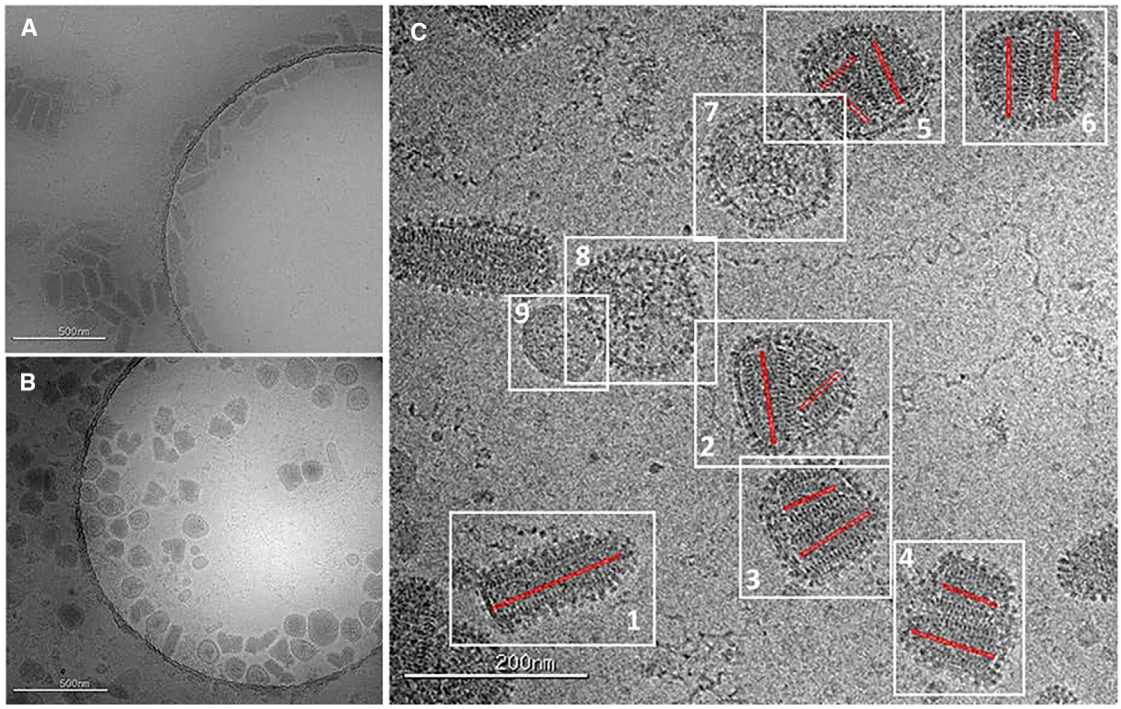

Figure 1. Cryo-EM images of VSV-GP samples

(A) Sample A with mostly B particles. (B) Sample B with morphologically different subpopulations at 28,000× magnification. (C) Sample B at 75,000× magnification. Packed or partially packed capsids of selected virus particles 1–6 are highlighted with red bars.

on the partial exclusion of analytes from the pores of the stationary phase. When coupled with a MALS detector, SEC provides a general approach for accurate analysis of size, molar mass, oligomeric state and aggregations of macromolecules.[33] Previous applications of SEC or SEC-MALS to viruses or viral vectors were focused on viral particle quantification, aggregation analysis, virus purification, and quantification of full versus empty viral vectors.[34–41] To the best of our knowledge, this work represents the first example demonstrating that SEC-MALS can differentiate between morphologically different viral particles through a shaped-based separation mechanism.

RESULTS

All VSV-GP samples in this study were prepared in early pre-clinical process development using different process parameters. Cryo-EM imaging of two representative VSV-GP samples, A and B, revealed distinct subpopulation profiles (Figure 1). In sample A (Figure 1A), most species are B particles in a preferential side-view orientation with an average length of about 190 nm and width of about 70 nm. This is consistent with the expected morphology of a VSV-type virus.[23] However, in sample B (Figure 1B), only a few B particles are present, while most particles are round or irregularly shaped with a size comparable to B particles. The nature of each sample and its subpopulations can be readily analyzed in higher-magnification images. In a representative image of sample B at 73,000× magnification (Figure 1C), in addition to the VSV-GP B particles (1), irregularly shaped particles with dense interior (2–6) and round/near-round particles with a lighter interior (7–9) were observed.

Table 1. Measured length of packed capsid segments

Particle	Segments (nm)	Total capsid length (nm)
1	–	150.7
2	99.8, 53.5	153.3
3	88.2, 58.0	146.2
4	93.0, 60.6	153.6
5	71.5, 46.4, 42.8	160.7
6	84.0, 73.9	157.9

Surface spikes with features of GP protein complexes described previously[23] are present in both B particles and irregularly shaped particles, suggesting that these subpopulations are related to VSV-GP. The interior striated pattern of B particle 1 (Figure 1C) is a characteristic feature of packed VSV ribonucleocapsids.[23] Inspection of the irregularly shaped particles showed that each block of the striated interior feature is consistent with a partially packed capsid, as highlighted by red bars in Figure 1C. To check the integrity of the viral genome, the length of each capsid segment was measured and is summarized in Table 1. The total capsid segment length of the irregularly shaped particles 2–6 matched well the total capsid length within B particle 1 (~150 nm), suggesting that the total genomic material is present in irregularly shaped particles. This is further supported by the

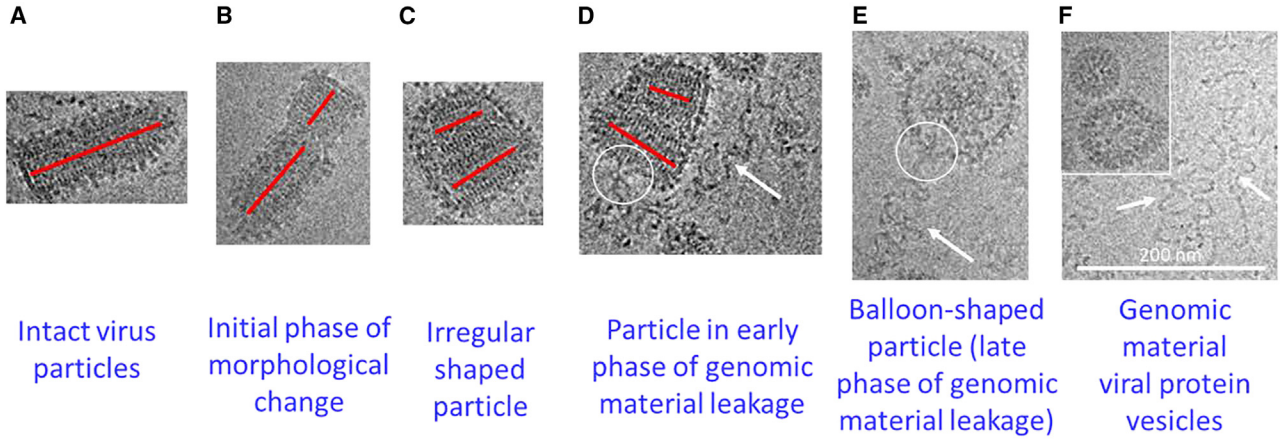

Figure 2. A spectrum of VSV-GP subpopulations in sample B

(A) B particle consistent with intact VSV-GP. (B) Particle with a near bullet shape morphology. (C) Irregularly shaped particle. (D) Irregularly shaped particle with a small extent of genomic material leakage. (E) Balloon-shaped particle with significant genomic material leakage. (F) Completely disrupted viral particles. White arrow, species consistent with VSV-GP genomic material.

observations that the envelope membrane of 2–6 was intact and that there was no visible leakage of genomic material. The irregular shape of the particle appears to be determined by the arrangement of rigid capsid fragments, while the soft membrane adapts to and maintains the overall shape of the particle.

Particles with round or near round morphology typically have a less dense interior (7–9), suggesting a lack of full-length genomic material inside the particles.[42] Most round particles have characteristic surface spikes of VSV-GP, and therefore these are likely empty or near-empty viral particles. This is further supported by thread-like species adjacent to the membrane of some balloon-shaped particles (7–8), which is consistent with features of unpacked genomic material.[21] A small fraction of round particles with light interior density (e.g., 9) were found to have a smooth surface and are most likely extracellular vesicles or exosomes derived from the host cell.

After analyzing more particles in cryo-EM images, we found additional species in between the subpopulation groups described above. There are particles with a near-bullet shape in which the capsid structure is already disturbed but has not fully become individual segments (Figure 2B). Moreover, irregularly shaped particles with a disturbed membrane and short tail-like species consistent with genomic material leakage are also present. Figure 2 shows the full spectrum of various subpopulations that are observed by cryo-EM.

Quantitative analysis by fraction counting of major subpopulation groups allows the comparison of subpopulation profiles between VSV-GP samples. To describe the particle morphologies observed, we define four subpopulations.

(1) Intact B particles: well-packed B particles that contain dense, striated interiors and are enclosed by a single lipid bilayer that is covered in spikes (Figure 2A).
(2) Near-B particles: intact particles that resemble a bullet shape with perturbations of striated interiors and are enclosed by a single lipid bilayer that is covered in spikes (Figure 2B).
(3) Irregularly shaped particles with a dense interior: intact particles that are round or irregular in shape, contain dense granular or striated interiors, and are enclosed by a single lipid bilayer that is covered in spikes (Figures 2C and 2D).
(4) Round or irregularly shaped particles with a less dense interior: intact particles that are round or irregular in shape, contain less dense granular interiors or are similar in density to that of the surrounding buffer, and are enclosed by a single lipid bilayer that is covered in spikes (Figures 2E and 2F).

Figure 3 shows the fraction counting analysis of five VSV-GP samples into the four defined morphologies. Sample A was found to contain 58% of B particles, a low percentage of near B particles, and an equal amount of irregularly shaped and empty particles, while sample B was composed mostly of irregularly shaped and empty particles with only 6% of B particles. The relative ratio of subpopulations varies significantly in some other samples, C–E, generated using different process parameters. Sample C features a near-equal amount of B particles and irregularly shaped particles, while D contains a high percentage of near-B particles. Samples B and E have similar percentages of B particles, but the ratio of round empty particles is higher in sample E.

To develop an orthogonal and high-throughput analytical method, we hypothesized that the morphology of particles with similar size and molecular weight may impact their interactions with the size exclusion chromatography stationary phase, particularly when the particle size is comparable to the pore size of the stationary phase (Figure 4B).

To test this hypothesis, SEC-MALS experiments were performed on multiple SEC columns (TSKgel G3000PW$_{XL}$, TSKgel G4000PW,

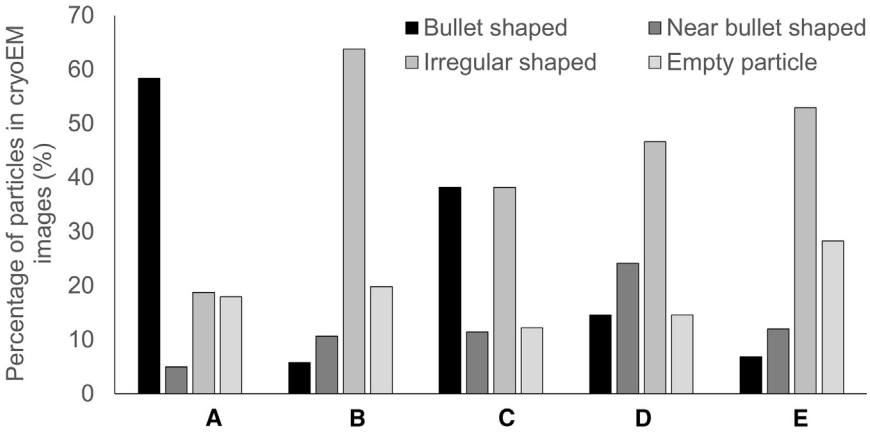

Figure 3. Fraction count of subpopulations in VSV-GP samples A–E

The number of particles used in each analysis is as follows: A, 646; B, 414; C, 262; D, 480; E, 743.

TSKgel G6000PW, and TSKgel G6000PW$_{XL}$, which are packed with the same type of resin but exhibit different pore and particle sizes). TSKgel G3000PW$_{XL}$ and TSKgel G4000PW have small pore sizes of approximately 20 and 50 nm, respectively, while TSKgel G6000PW$_{XL}$ has been reported to have a large pore diameter of 250 nm.[39] To check the morphology effect on the SEC profile, sample A with a high percentage of B particles and sample B with mostly irregularly shaped particles were employed in SEC method development. The majority of near-B particles and irregularly shaped particles in sample B were found to have intact lipid membranes, total genomic material, and viral proteins within the particle, so the molecular weights of these subpopulations are comparable to B particles in A. SEC-MALS chromatography using TSKgel G3000PW$_{XL}$ yielded sharp peaks with a near-identical elution volume and peak shape detected by static light scattering at 90° for samples A (Figure 5A, trace A-1) and B (Figure 5A, trace B-1). Similar chromatograms were obtained using TSKgel G4000PW (Figure S1). In contrast, sample B (Figure 5A, trace B-2), with mostly irregularly shaped viral particles, showed a significant shift in peak maximum and a broadened peak compared with sample A (Figure 5A, trace A-2) when analyzed on TSKgel G6000PW$_{XL}$. Peak broadening was also observed using a TSKgel G6000PW column, although the difference between samples A and B was less pronounced (Figure S1). The strong light scattering and UV absorption ratio (A_{260}/A_{280}) of the peaks were consistent with virus particles containing both protein and nucleic acid. These observations showed that an appropriate SEC method can differentiate VSV-GP samples with different morphological profiles.

To investigate whether the observed peak broadening was caused by morphologically different subpopulations or by sample overloading, a serial dilution experiment was performed on sample B. The static light scattering intensity decreased according to the dilution factor applied to the original sample (Figure 5B). If the light scattering profile was individually normalized, then the peak broadening profiles were identical in the original and samples diluted by 50 times (Figure 5C), suggesting that the peak tailing was caused by subpopulations in the sample and not chromatography artifacts. Further experiments also confirmed that peak shape was independent of sample injection volume (data not shown). Therefore, a broadened peak profile in SEC-MALS was the characteristic feature of sample B, and individually normalized SEC profiles detected by static light scattering at 90° (LS90) can be directly compared for samples within about two orders of magnitude concentration range.

Angular dependence of the scattered light in MALS allows for sizing of particles.[43] Sample A provided a rms (root mean square) radius (or radius of gyration) at about 71 nm, consistent with the size of VSV-GP viral particles. For sample B, the rms radius ranged from about 73 nm at the front of the SEC peak to 65 nm at the tail, consistent with a higher proportion of morphological subpopulations (Figure 5A, dashed line). This observation differed from dynamic light scattering measurement of particle sizes in bulk sample solution, where both samples A and B yielded similar hydrodynamic radii at 78 nm. These data suggest that the SEC separation mechanism is based on differences in radius of gyration, which are related to the shape of viral particles.

To better understand the degree of separation between particles with different morphologies, fractions at the front (16–17 min), center (18–19 min), and tail (20–23 min) of the SEC-MALS peak of sample B were collected, concentrated, and imaged by cryo-EM. In all of these fractions, viral particles were readily visible. The fraction of the peak front contained a higher percentage of B particles or near-B particles (49%) compared with the load material sample B (16%), while the peak tail (20–23 min) consisted of nearly all round and irregularly shaped particles (Figure 5D). The results suggest that, despite the low resolution, SEC fractionation allowed the enrichment of morphologically different subpopulations, further supporting a separation mechanism based on particle morphology.

Besides particle morphology analysis, SEC-MALS enables the analysis of residual impurities or formulation components in virus preparations and quantification of virus particles when UV chromatograms are also considered, as shown in our previous study.[44] The separation of viral particles from proteins using the SEC method in this work was demonstrated by the SEC-UV-MALS profile of a mixture of sample B with BSA (Figure S2A). The light scattering detection was more sensitive to large virus particles, while UV detection readily revealed the presence of other UV active species in the sample (Figures S2B and S2C). Therefore, the combination of light scattering and UV profiles offers a more comprehensive characterization of virus samples.

Application of SEC-MALS to virus particle morphology analysis was further demonstrated with more virus samples in different

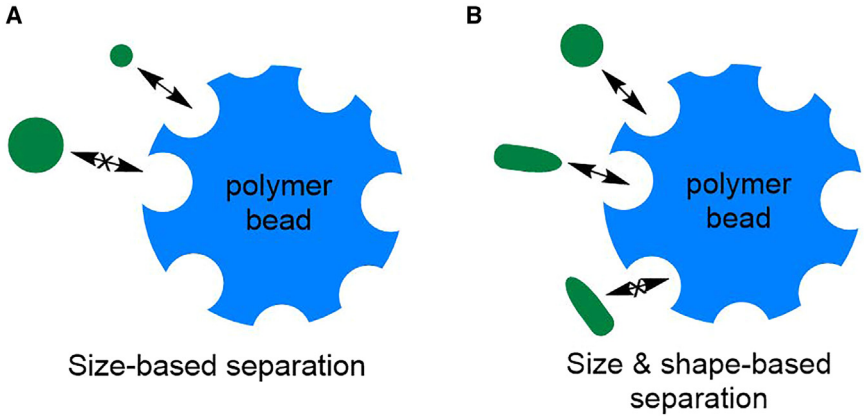

Figure 4. Separation mechanisms in SEC chromatography

(A) Size-based separation mechanism. (B) Hypothesis of a size- and shape-based separation mechanisms.

formulations, and SEC-MALS peak shape was shown to correlate well with sample subpopulation profile. Figure 6A plots the SEC-MALS LS90 profile of the five VSV-GP samples, A–E, described in Figure 3. The extent of peak broadening and shift was consistent with the subpopulation fraction counting analysis for the five samples, with sample B having the highest percentage of non-B particles and, therefore, the broadest SEC peak. Only minor but reproducible differences were observed for samples A, C, and D, although the percentages of intact bullet shaped particles were 58%, 38%, and 15%, respectively. This can be attributed to the presence of large numbers of near-B particles in samples C and D that may interact with the SEC stationary phase similarly as intact B particles and that are therefore indistinguishable from B particles in SEC. Therefore, SEC-MALS peak broadening is sensitive to the presence of round and irregularly shaped particles, consistent with a morphology-based separation mechanism.

SEC-MALS peak broadening can be measured by peak full width at half maximum peak height (FWHM). Figure 6B plots the percentage of round and irregularly shaped particles from cryo-EM imaging of 12 samples against FWHM in the SEC-MALS LS90 chromatogram. A good non-linear correlation was observed, suggesting that SEC-MALS is a robust orthogonal method to characterize VSV-GP particle morphology.

DISCUSSION

Morphological subpopulations of VSV-GP particles were systematically investigated in the study. A spectrum of subpopulations with different morphology was observed in certain VSV-GP samples, and detailed structural features of these species were readily visible from high-resolution cryo-EM imaging. The characteristics of some subpopulations, such as morphologically distorted particles, are consistent with previous findings with negative staining TEM,[20] but high-resolution cryo-EM imaging enables the study of fine structure details, such as the interior features and membrane integrity of these subpopulations. Moreover, in contrast to negative staining TEM, cryo-EM sample preparation does not require sample staining, and the vitrification process embeds virus particles in a thin layer of amorphous ice with only minimal perturbation of the native state of the virus particles in sample grid preparation. Overall, cryo-EM is superior to negative staining TEM when studying the structure of VSV-GP subpopulations.[45,46]

Cryo-EM provides high-resolution and information-rich images for VSV-GP subpopulation analysis, but a high viral particle concentration (10^{11}–10^{12} particles/mL) is required for reliable analysis of subpopulation profile. Some excipients commonly used in formulations, such as sugar or sugar derivatives, may also lower the contrast of the cryo-EM images. In addition, the high cost and low throughput of cryo-EM make it an unfavorable method for routine analysis of VSV-GP samples when higher sensitivity or faster analysis is needed.

The SEC-MALS method developed in this work serves as an alternative method to cryo-EM. Since different subpopulations have similar sizes, and they usually form a continuous spectrum of morphology, it is not feasible to fully separate B particles and non-B particles with the current method. Instead, peak shifting and broadening correlate well with the presence of non-B particles. Better resolution can be achieved with TSKgel G6000PW$_{XL}$ (13 μm) than with the TSKgel G6000PW (17 μm) column, suggesting that the particle size and possibly the inter-particle channels of the stationary phase will also influence the separation. Using a calibration curve prepared with samples that have different ratios of the subpopulations (Figure 6), SEC-MALS can also semiquantitatively measure the ratio of B to non-B particles.

The resolution of subpopulation separation in SEC-MALS is low, but the method enables high-throughput particle morphology and purity analysis of VSV-GP samples. In addition, the high sensitivity of SEC-MALS against virus particles allows the analysis of virus samples at as low as 10^8 particles/mL, which is approximately two to three orders of magnitude lower than the minimal sample concentration for cryo-EM imaging. The increased sensitivity enables the analysis of less concentrated virus samples from process development.

We showed that morphologically different VSV-GP particles can be enriched by fractionation of the broadened SEC peak (Figure 5D). B particles elute mostly in the front of the broadened peak, suggesting less interactions with the stationary phase, while irregularly shaped and round particles have more retention on the column. This observation is consistent with the proposed model (Figure 4B) where surface pores of the stationary phase are more accessible to round particles and morphologically different particles can be partially separated based on shape. So, in addition to being a characterization method, the SEC-MALS method also serves as a simple approach to enrich the morphologically different VSV-GP particles from a single

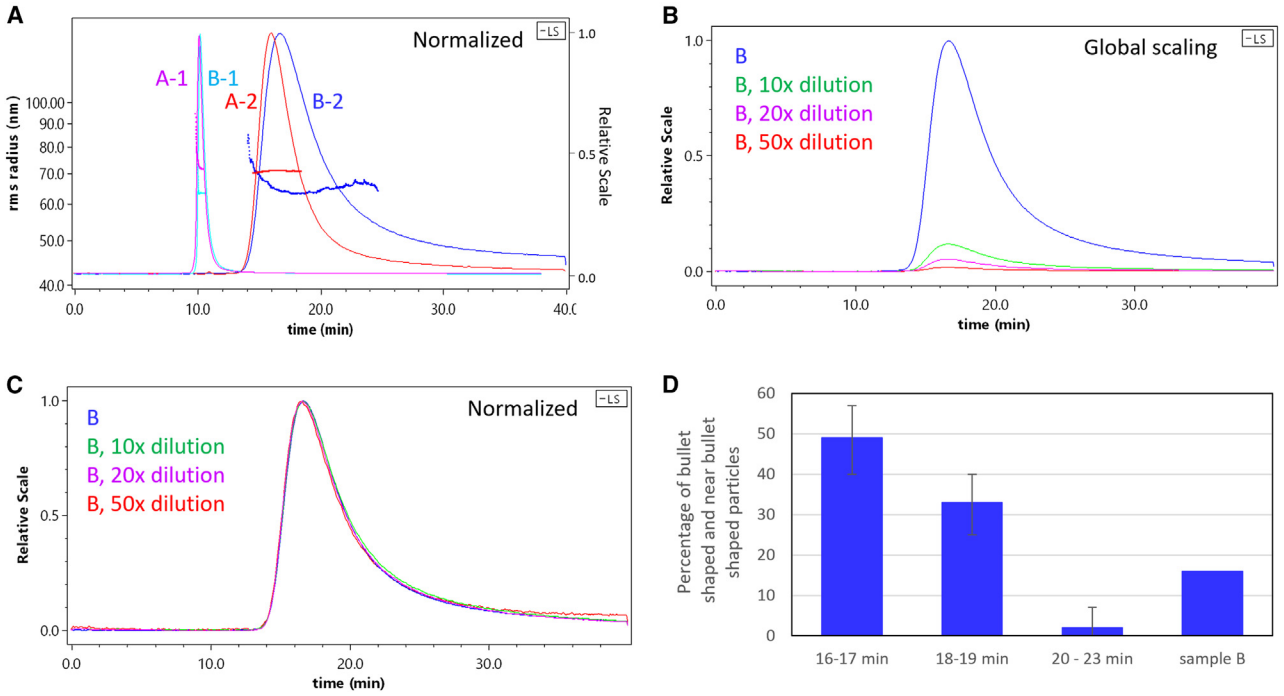

Figure 5. SEC-MALS method development

(A) Individually scaled peak profiles of samples A and B with TSKgel G3000PWXL (A-1 and B-1) and TSKgel G6000PWXL (A-2 and B-2) columns. (B and C) Globally scaled (B) and individually scaled (C) SEC-MALS peak profiles of sample B diluted by 0, 10, 20, and 50 times with the mobile phase. 90° static light scattering (LS90) profiles were employed in all comparisons. (D) Percentage of B particles and near-B particles for sample B load material; fractions were collected at 16–17, 18–19, and 20–23 min during SEC chromatography of sample B, measured by fraction counting of cryo-EM images. Error bars were calculated by fraction counting of images from three grid preparations.

VSV-GP sample on a small scale, which is difficult to achieve by other separation methods.

In summary, the characterization of VSV-GP morphology can be achieved when combining the high resolution of cryo-EM imaging and high throughput of SEC-MALS. We envision that the two complementary methods will also be applicable to morphological analysis of other non-spherical viruses or nanoparticles.

MATERIALS AND METHODS

VSV-GP samples

VSV-GP particles were propagated in HEK293-F cells. After infection, the harvest was clarified by centrifugation at 2,000 × *g* for 5 min. The supernatant was treated with 200 mM NaCl, filtered using a 0.22 μm filter, and then treated with nuclease to reduce the host cell DNA content. The virus material was then diluted 1:1 with 100 mM Tris-HCl (pH 7.5) before proceeding with downstream processing. The virus material was subsequently purified by downstream unit operations, including ion exchange chromatography and tangential flow ultrafiltration, similar to a method published previously.[47] All VSV-GP samples, including A–E, were produced in early pre-clinical process development using different upstream and downstream process parameters. Infectious virus titer, virus genome copies, and virus particle counts were measured using methods published previously.[48]

Cryo-EM

Cryo-EM imaging data collection was performed by NanoImaging Services.

Each sample was preserved in vitrified ice supported by holey carbon films on 400-mesh copper grids. Each sample was prepared by applying a 3 μL drop of sample suspension to a cleaned grid, blotting away with filter paper, and immediately proceeding with vitrification in liquid ethane. EM was performed using a Thermo Fisher Scientific Glacios cryotransmission electron microscope operated at 200 kV and equipped with a Falcon 3 direct electron detector. Vitreous ice grids were clipped into cartridges and transferred into a cassette and then into the Glacios autoloader, all while maintaining the grids at cryogenic temperature (below −170°C). Automated data collection was carried out using Leginon software,[49] where high-magnification movies are acquired by selecting targets at a lower magnification.

Images of each grid were acquired at multiple scales to assess the overall distribution of the specimen. After identifying potentially suitable target areas for imaging at lower magnifications, high-magnification images were acquired at nominal magnifications of 150,000× (0.10 nm/pixel), 73,000× (0.20 nm/pixel), and 28,000× (0.52 nm/pixel). The images were acquired at a nominal underfocus of −5.5 to −2.5 μm and electron doses of ∼10–25 $e^{-}/Å^{2}$.

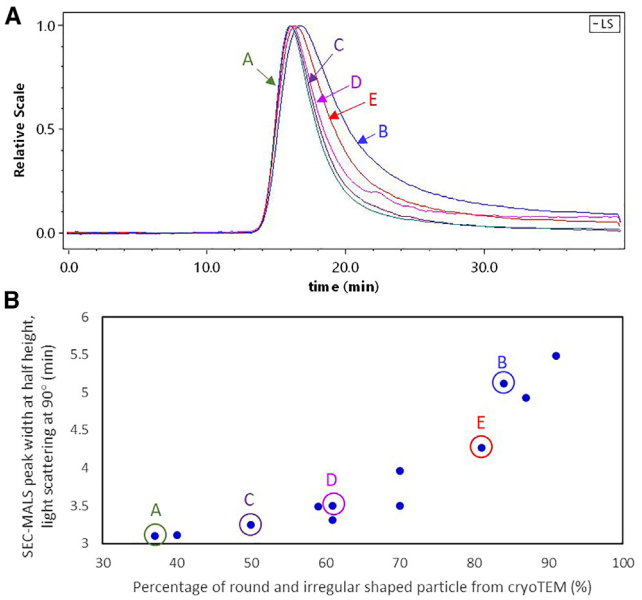

Figure 6. Correlation of SEC-MALS profile with cryo-EM imaging

(A) SEC LS90 profile of five different VSV-GP samples. (B) Correlation of SEC-MALS peak broadening measured by peak width at half-height with percentage of round and irregularly shaped particles from cryo-EM imaging.

Fraction counting of subpopulations

VSV-GP-related particles had to have a minimum length of 50 nm to be included in the fraction counting analysis. At least 200 particles were randomly selected from a random subset of images at 28,000× magnification. The particles were sorted into four morphology subpopulation categories as defined in the text.

SEC-MALS

In SEC-MALS analysis, samples were injected through an Agilent HPLC (high-performance liquid chromatography) system with UV detection coupled with a DAWN HELOS-II multiangle light scattering detector (Wyatt Technology, Santa Barbara, CA, USA) with a built-in QELS (quasi-elastic light scattering) dynamic light scattering (DLS) detector and an Optilab T-rex RI (refractive index) detector. Virus subpopulation analyses were performed on a TSKgel 6000 PW_{XL} SEC column (13 µm, 30 cm × 7.8 mm, TOSOH Bioscience), TSKgel 6000 PW SEC column (17 µm, 30 cm × 7.5 mm, TOSOH Bioscience), TSKgel 4000 PW SEC column (17 µm, 30 cm × 7.5 mm, TOSOH Bioscience), or TSKgel 3000 PW_{XL} SEC column (7 µm, 30 cm × 7.8 mm, TOSOH Bioscience) operated at room temperature with an isocratic flow rate of 0.5 mL/min using a mobile phase composed of PBS or a buffer system suitable for the virus to be analyzed.[40] Unless otherwise mentioned, the injection volume was 40 µL. The UV detector was operated at 280 nm wavelength. ASTRA v.7.3 software was used for acquiring and analyzing UV, RI, and MALS data.

The MALS data were analyzed, and the rms radius was calculated with the instrumental software Astra v.7.3 following a procedure described previously for AAV (adeno-associated viruses).[35] The calculated specific refractive index increment (dn/dc) of VSV-GP was 0.173, which is based on the concentration weighted average of virion components using the reported composition of VSV[50] and intrinsic dn/dc values of 0.185, 0.170, and 0.130 for viral proteins, nucleic acid, and lipid.

SEC fractionation

Fractions of the SEC-MALS peak were manually collected 10 times at elution times of 16–17, 18–19, and 20–23 min during SEC-MALS chromatography of sample B. The material of fractions at each time slice was combined and concentrated by centrifugation at 19,000 × *g* for 2 h at 4°C. The supernatant was discarded, and the residual material was redispersed in 50 µL of buffer for cryo-EM imaging. Fraction counting analysis was performed with cryo-EM images acquired at 8,500× magnification.

Particle size measurement by DLS

A Dynapro Plate Reader III (Wyatt Technology) was utilized to determine the hydrodynamic radius (r_h) of viral particles. All measurements were performed on 384-well microtiter plates (Greiner, Bio-one) at room temperature. 60 µL sample was carefully added to the wells, and the plate was centrifuged at 400 × *g* for 1 min prior to loading into the plate reader. Data analysis was performed with Dynamics software, utilizing the autocorrelation function to determine quality of data. The r_h distribution of peaks was calculated using regularization fit.

DATA AVAILABILITY

All data used to evaluate the conclusions of the article are present in the paper and/or the supplemental information.

ACKNOWLEDGMENTS

We thank Ramona Businger, Martin Dass, Mohamed Abdellatif, Claudia Simon, Till Wenger, Ingo Gorr, Yoo-Chun Kim, Vladimir Papov, Kerstin Schaefer, and Andreas Funkner for discussions and support. We thank Amy Gao for assistance with the project. We thank NanoImaging Services for performing cryo-EM experiments. This work is funded entirely by Boehringer Ingelheim Pharmaceuticals, Inc.

AUTHOR CONTRIBUTIONS

D.X., M.H., X.H., J.S., T.A., T.K., J.A., A.V., D. Hochdorfer, and A.S designed and discussed the experiments. D.X., L.K., K.B., and A.S. performed the experiments. R.D., T.A., M.B., D. Hotter, S.G., and T.K. provided the VSV-GP samples used in the study. D.X. wrote the manuscript with support and feedback from the other others. All authors contributed to data analyses. All authors contributed to reviewing and revising the manuscript.

DECLARATION OF INTERESTS

The authors are/were employed at Boehringer Ingelheim Pharmaceuticals, Boehringer Ingelheim Pharma GmbH & Co. KG, or ViraTherapeutics GmbH at the time of the experiments.

SUPPLEMENTAL INFORMATION

Supplemental information can be found online at https://doi.org/10.1016/j.omtm.2025.101429.

REFERENCES

1. Lawler, S.E., Speranza, M.-C., Cho, C.-F., and Chiocca, E.A. (2017). Oncolytic Viruses in Cancer Treatment: A Review. JAMA Oncol. *3*, 841–849. https://doi.org/10.1001/jamaoncol.2016.2064.
2. Fukuhara, H., Ino, Y., and Todo, T. (2016). Oncolytic virus therapy: A new era of cancer treatment at dawn. Cancer Sci. *107*, 1373–1379. https://doi.org/10.1111/cas.13027.
3. Muik, A., Stubbert, L.J., Jahedi, R.Z., Geiß, Y., Kimpel, J., Dold, C., Tober, R., Volk, A., Klein, S., Dietrich, U., et al. (2014). Re-engineering Vesicular Stomatitis Virus to Abrogate Neurotoxicity, Circumvent Humoral Immunity, and Enhance Oncolytic Potency. Cancer Res. *74*, 3567–3578. https://doi.org/10.1158/0008-5472.can-13-3306.
4. Muik, A., Dold, C., Geiß, Y., Volk, A., Werbizki, M., Dietrich, U., and Laer, D. von (2012). Semireplication-competent vesicular stomatitis virus as a novel platform for oncolytic virotherapy. J. Mol. Medicine Berlin Ger. *90*, 959–970. https://doi.org/10.1007/s00109-012-0863-6.
5. Schreiber, L.-M., Urbiola, C., Das, K., Spiesschaert, B., Kimpel, J., Heinemann, F., Stierstorfer, B., Müller, P., Petersson, M., Erlmann, P., et al. (2019). The lytic activity of VSV-GP treatment dominates the therapeutic effects in a syngeneic model of lung cancer. Br. J. Cancer *121*, 647–658. https://doi.org/10.1038/s41416-019-0574-7.
6. Muik, A., Kneiske, I., Werbizki, M., Wilflingseder, D., Giroglou, T., Ebert, O., Kraft, A., Dietrich, U., Zimmer, G., Momma, S., and von Laer, D. (2011). Pseudotyping Vesicular Stomatitis Virus with Lymphocytic Choriomeningitis Virus Glycoproteins Enhances Infectivity for Glioma Cells and Minimizes Neurotropism. J. Virol. *85*, 5679–5684. https://doi.org/10.1128/jvi.02511-10.
7. Hastie, E., and Grdzelishvili, V.Z. (2012). Vesicular stomatitis virus as a flexible platform for oncolytic virotherapy against cancer. J. Gen. Virol. *93*, 2529–2545. https://doi.org/10.1099/vir.0.046672-0.
8. Tober, R., Banki, Z., Egerer, L., Muik, A., Behmüller, S., Kreppel, F., Greczmiel, U., Oxenius, A., von Laer, D., and Kimpel, J. (2014). VSV-GP: a Potent Viral Vaccine Vector That Boosts the Immune Response upon Repeated Applications. J. Virol. *88*, 4897–4907. https://doi.org/10.1128/jvi.03276-13.
9. Kimpel, J., Urbiola, C., Koske, I., Tober, R., Banki, Z., Wollmann, G., and von Laer, D. (2018). The Oncolytic Virus VSV-GP Is Effective against Malignant Melanoma. Viruses *10*, 108. https://doi.org/10.3390/v10030108.
10. Urbiola, C., Santer, F.R., Petersson, M., van der Pluijm, G., Horninger, W., Erlmann, P., Wollmann, G., Kimpel, J., Culig, Z., and von Laer, D. (2018). Oncolytic activity of the rhabdovirus VSV-GP against prostate cancer. Int. J. Cancer *143*, 1786–1796. https://doi.org/10.1002/ijc.31556.
11. Dold, C., Rodriguez Urbiola, C., Wollmann, G., Egerer, L., Muik, A., Bellmann, L., Fiegl, H., Marth, C., Kimpel, J., and von Laer, D. (2016). Application of interferon modulators to overcome partial resistance of human ovarian cancers to VSV-GP oncolytic viral therapy. Mol. Ther. Oncolytics *3*, 16021. https://doi.org/10.1038/mto.2016.21.
12. Green, T.J., Zhang, X., Wertz, G.W., and Luo, M. (2006). Structure of the Vesicular Stomatitis Virus Nucleoprotein-RNA Complex. Science *313*, 357–360. https://doi.org/10.1126/science.1126953.
13. Ding, H., Green, T.J., Lu, S., and Luo, M. (2006). Crystal Structure of the Oligomerization Domain of the Phosphoprotein of Vesicular Stomatitis Virus. J. Virol. *80*, 2808–2814. https://doi.org/10.1128/jvi.80.6.2808-2814.2006.
14. Gaudier, M., Gaudin, Y., and Knossow, M. (2002). Crystal structure of vesicular stomatitis virus matrix protein. EMBO J. *21*, 2886–2892. https://doi.org/10.1093/emboj/cdf284.
15. Graham, S.C., Assenberg, R., Delmas, O., Verma, A., Gholami, A., Talbi, C., Owens, R.J., Stuart, D.I., Grimes, J.M., and Bourhy, H. (2008). Rhabdovirus Matrix Protein Structures Reveal a Novel Mode of Self-Association. PLoS Pathog. *4*, e1000251. https://doi.org/10.1371/journal.ppat.1000251.
16. Green, T.J., and Luo, M. (2009). Structure of the vesicular stomatitis virus nucleocapsid in complex with the nucleocapsid-binding domain of the small polymerase cofactor, P. Proc. Natl. Acad. Sci. USA *106*, 11713–11718. https://doi.org/10.1073/pnas.0903228106.
17. Roche, S., Bressanelli, S., Rey, F.A., and Gaudin, Y. (2006). Crystal Structure of the Low-pH Form of the Vesicular Stomatitis Virus Glycoprotein G. Science *313*, 187–191. https://doi.org/10.1126/science.1127683.
18. Leyrat, C., Yabukarski, F., Tarbouriech, N., Ribeiro, E.A., Jensen, M.R., Blackledge, M., Ruigrok, R.W.H., and Jamin, M. (2011). Structure of the Vesicular Stomatitis Virus N0-P Complex. PLoS Pathog. *7*, e1002248. https://doi.org/10.1371/journal.ppat.1002248.
19. Roche, S., Rey, F.A., Gaudin, Y., and Bressanelli, S. (2007). Structure of the Prefusion Form of the Vesicular Stomatitis Virus Glycoprotein G. Science *315*, 843–848. https://doi.org/10.1126/science.1135710.
20. Howatson, A.F., and Whitmore, G.F. (1962). The development and structure of vesicular stomatitis virus. Virology *16*, 466–478. https://doi.org/10.1016/0042-6822(62)90228-3.
21. Nakai, T., and Howatson, A.F. (1968). The fine structure of vesicular stomatitis virus. Virology *35*, 268–281. https://doi.org/10.1016/0042-6822(68)90267-5.
22. Petric, M., and Prevec, L. (1970). Vesicular stomatitis virus—A new interfering particle, intracellular structures, and virus-specific RNA. Virology *41*, 615–630. https://doi.org/10.1016/0042-6822(70)90427-7.
23. Ge, P., Tsao, J., Schein, S., Green, T.J., Luo, M., and Zhou, Z.H. (2010). Cryo-EM Model of the Bullet-Shaped Vesicular Stomatitis Virus. Science *327*, 689–693. https://doi.org/10.1126/science.1181766.
24. Desfosses, A., Ribeiro, E.A., Schoehn, G., Blondel, D., Guilligay, D., Jamin, M., Ruigrok, R.W.H., and Gutsche, I. (2013). Self-organization of the vesicular stomatitis virus nucleocapsid into a bullet shape. Nat. Commun. *4*, 1429. https://doi.org/10.1038/ncomms2435.
25. Liang, B., Li, Z., Jenni, S., Rahmeh, A.A., Morin, B.M., Grant, T., Grigorieff, N., Harrison, S.C., and Whelan, S.P.J. (2015). Structure of the L Protein of Vesicular Stomatitis Virus from Electron Cryomicroscopy. Cell *162*, 314–327. https://doi.org/10.1016/j.cell.2015.06.018.
26. Si, Z., Zhou, K., Tsao, J., Luo, M., and Zhou, Z.H. (2022). Locations and in situ structure of the polymerase complex inside the virion of vesicular stomatitis virus. Proc. Natl. Acad. Sci. USA *119*, e2111948119. https://doi.org/10.1073/pnas.2111948119.
27. Jenni, S., Horwitz, J.A., Bloyet, L.-M., Whelan, S.P.J., and Harrison, S.C. (2022). Visualizing molecular interactions that determine assembly of a bullet-shaped vesicular stomatitis virus particle. Nat. Commun. *13*, 4802. https://doi.org/10.1038/s41467-022-32223-1.
28. Zhou, K., Si, Z., Ge, P., Tsao, J., Luo, M., and Zhou, Z.H. (2022). Atomic model of vesicular stomatitis virus and mechanism of assembly. Nat. Commun. *13*, 5980. https://doi.org/10.1038/s41467-022-33664-4.
29. Huang, A.S., and Wagner, R.R. (1966). Defective T particles of vesicular stomatitis virus II. Biologic role in homologous interference. Virology *30*, 173–181. https://doi.org/10.1016/0042-6822(66)90093-6.
30. PREVEC, L., and KANG, C.Y. (1970). Homotypic and Heterotypic Interference by Defective Particles of Vesicular Stomatitis Virus. Nature *228*, 25–27. https://doi.org/10.1038/228025a0.
31. Holland, J.J., and Villarreal, L.P. (1974). Persistent Noncytocidal Vesicular Stomatitis Virus Infections Mediated by Defective T Particles that Suppress Virion Transcriptase. Proc. Natl. Acad. Sci. USA *71*, 2956–2960. https://doi.org/10.1073/pnas.71.8.2956.
32. Holland, J.J., Villarreal, L.P., and Breindl, M. (1976). Factors involved in the generation and replication of rhabdovirus defective T particles. J. Virol. *17*, 805–815. https://doi.org/10.1128/jvi.17.3.805-815.1976.
33. Sahin, E., and Roberts, C.J. (2012). Size-Exclusion Chromatography with Multi-angle Light Scattering for Elucidating Protein Aggregation Mechanisms. In Therapeutic Proteins - Methods and Protocols, V. Voynov and J.A. Caravella, eds. (Humana Press), pp. 403–423. https://doi.org/10.1007/978-1-61779-921-1_25.
34. Transfiguracion, J., Jaalouk, D.E., Ghani, K., Galipeau, J., and Kamen, A. (2003). Size-Exclusion Chromatography Purification of High-Titer Vesicular Stomatitis Virus G Glycoprotein-Pseudotyped Retrovectors for Cell and Gene Therapy Applications. Hum. Gene Ther. *14*, 1139–1153. https://doi.org/10.1089/104303403322167984.
35. McIntosh, N.L., Berguig, G.Y., Karim, O.A., Cortesio, C.L., De Angelis, R., Khan, A.A., Gold, D., Maga, J.A., and Bhat, V.S. (2021). Comprehensive characterization

and quantification of adeno associated vectors by size exclusion chromatography and multi angle light scattering. Sci. Rep. *11*, 3012. https://doi.org/10.1038/s41598-021-82599-1.

36. Meng, H., Sorrentino, M., Woodcock, D., O'Riordan, C., Dhawan, V., Verhagen, M., and Davies, C. (2022). Size Exclusion Chromatography with Dual Wavelength Detection as a Sensitive and Accurate Method for Determining the Empty and Full Capsids of Recombinant Adeno-Associated Viral Vectors. Hum. Gene Ther. *33*, 202–212. https://doi.org/10.1089/hum.2021.123.

37. Transfiguracion, J., Jorio, H., Meghrous, J., Jacob, D., and Kamen, A. (2007). High yield purification of functional baculovirus vectors by size exclusion chromatography. J. Virol. Methods *142*, 21–28. https://doi.org/10.1016/j.jviromet.2007.01.002.

38. Heider, S., Muzard, J., Zaruba, M., and Metzner, C. (2017). Integrated Method for Purification and Single-Particle Characterization of Lentiviral Vector Systems by Size Exclusion Chromatography and Tunable Resistive Pulse Sensing. Mol. Biotechnol. *59*, 251–259. https://doi.org/10.1007/s12033-017-0009-8.

39. Vajda, J., Weber, D., Brekel, D., Hundt, B., and Müller, E. (2016). Size distribution analysis of influenza virus particles using size exclusion chromatography. J. Chromatogr. A *1465*, 117–125. https://doi.org/10.1016/j.chroma.2016.08.056.

40. Schimek, A., Ng, J.K.M., Basbas, I., Martin, F., Xin, D., Saleh, D., and Hubbuch, J. (2024). An HPLC-SEC-based rapid quantification method for vesicular stomatitis virus particles to facilitate process development. Mol. Ther. Methods Clin. Dev. *32*, 101252. https://doi.org/10.1016/j.omtm.2024.101252.

41. Steppert, P., Burgstaller, D., Klausberger, M., Tover, A., Berger, E., and Jungbauer, A. (2017). Quantification and characterization of virus-like particles by size-exclusion chromatography and nanoparticle tracking analysis. J. Chromatogr. A *1487*, 89–99. https://doi.org/10.1016/j.chroma.2016.12.085.

42. Stagg, S.M., Yoshioka, C., Davulcu, O., and Chapman, M.S. (2022). Cryo-electron Microscopy of Adeno-associated Virus. Chem. Rev. *122*, 14018–14054. https://doi.org/10.1021/acs.chemrev.1c00936.

43. Minton, A.P. (2016). Recent applications of light scattering measurement in the biological and biopharmaceutical sciences. Anal. Biochem. *501*, 4–22. https://doi.org/10.1016/j.ab.2016.02.007.

44. Gautam, S., Xin, D., Garcia, A.P., and Spiesschaert, B. (2022). Single-step rapid chromatographic purification and characterization of clinical stage oncolytic VSV-GP. Front. Bioeng. Biotechnol. *10*, 992069. https://doi.org/10.3389/fbioe.2022.992069.

45. Nogales, E., and Scheres, S.H.W. (2015). Cryo-EM: A Unique Tool for the Visualization of Macromolecular Complexity. Mol. Cell *58*, 677–689. https://doi.org/10.1016/j.molcel.2015.02.019.

46. Luque, D., and Castón, J.R. (2020). Cryo-electron microscopy for the study of virus assembly. Nat. Chem. Biol. *16*, 231–239. https://doi.org/10.1038/s41589-020-0477-1.

47. Ausubel, L.J., Meseck, M., Derecho, I., Lopez, P., Knoblauch, C., McMahon, R., Anderson, J., Dunphy, N., Quezada, V., Khan, R., et al. (2011). Current Good Manufacturing Practice Production of an Oncolytic Recombinant Vesicular Stomatitis Viral Vector for Cancer Treatment. Hum. Gene Ther. *22*, 489–497. https://doi.org/10.1089/hum.2010.159.

48. Dambra, R., Matter, A., Graca, K., Akhand, S.S., Mehta, S., Bell-Cohn, A., Swenson, J.M., Abid, S., Xin, D., Lewis, C., et al. (2023). Nonclinical pharmacokinetics and biodistribution of VSV-GP using methods to decouple input drug disposition and viral replication. Mol. Ther. Methods Clin. Dev. *28*, 190–207. https://doi.org/10.1016/j.omtm.2022.12.013.

49. Suloway, C., Pulokas, J., Fellmann, D., Cheng, A., Guerra, F., Quispe, J., Stagg, S., Potter, C.S., and Carragher, B. (2005). Automated molecular microscopy: The new Leginon system. J. Struct. Biol. *151*, 41–60. https://doi.org/10.1016/j.jsb.2005.03.010.

50. Thomas, D., Newcomb, W.W., Brown, J.C., Wall, J.S., Hainfeld, J.F., Trus, B.L., and Steven, A.C. (1985). Mass and molecular composition of vesicular stomatitis virus: a scanning transmission electron microscopy analysis. J. Virol. *54*, 598–607.